Highlights

Numerical predictions of intralaminar and interlaminar damage in thin composite shells subjected to impact loads

L.M. Ferreira, C.A.C.P. Coelho, P.N.B. Reis

- Investigation of the impact dynamics on composite shells using the explicit finite element method.
- Numerical predictions of intralaminar damage using a continuum damage mechanics model.
- Numerical predictions of interlaminar damage using a surface-based cohesive model.
- Prediction of energy dissipation forms for different thicknesses.

Numerical predictions of intralaminar and interlaminar damage in thin composite shells subjected to impact loads

L.M. Ferreira[a,b,*], C.A.C.P. Coelho[c], P.N.B. Reis[d]

[a] *Grupo de Elasticidad y Resistencia de Materiales. Escuela Técnica Superior de Ingeniería. Universidad de Sevilla. Camino Descubrimientos, S/N 41092 Sevilla. España*

[b] *Escuela Politécnica Superior. Universidad de Sevilla. C/ Virgen de África, 7, Sevilla, 41011. España*

[c] *Unidade Departamental de Engenharias. Escola Superior de Tecnologia de Abrantes. Instituto Politécnico de Tomar. Rua 17 de Agosto de 1808 S/N 2200-370 Abrantes. Portugal*

[d] *University of Coimbra, CEMMPRE, ARISE, Department of Mechanical Engineering, 3030-194 Coimbra, Portugal*

Abstract

This paper investigates the impact dynamics of thin semicylindrical woven composite laminate shells, with a particular focus on understanding the influence of thickness. Utilising the finite element (FE) method, the study evaluates both intralaminar and interlaminar damage associated with the impact response. The findings show that the implementation of the explicit FE method, along with a continuum damage mechanics model, for the intralaminar damage, and a surface-based cohesive model, for the interlaminar damage, may be used to correctly predict the load histories, as well as the maximum impact force, maximum displacement, contact time and impact bending stiffness (IBS). The numerical predictions reproduce well the linear response of the maximum impact force and maximum displacement to the thickness variation, as well as the 2^{nd} order polynomial curve of the IBS, with errors ranging from 2.7% to 15.9%. Moreover, the damage areas and the effect of thickness on the damage severity were accurately replicated. These results' validation enables the prediction of the energy histories and the ensuing energy dissipation forms. According to the findings, the intralaminar damage is around 5 times more significant than the other energy dissipation forms. The accuracy of the simulation creates the possibility for more impact investigations using a similar numerical approach, reducing the expenditures of experimental testing.

Keywords: Finite element method (FEM), Continuum damage mechanics (CDM), Cohesive behaviour, Low-velocity impact, Woven-fabric composites, Composite shells

1. Introduction

Composite materials have become increasingly popular due to their unique combination of high strength, low weight, and excellent fatigue resistance. However, they are susceptible to damage from low-velocity impacts that can occur during handling, transportation, maintenance, and service. These impacts can cause localised damage to the structure, which can result in reduced strength, stiffness, and durability of the composite material [1–5]. Therefore, understanding the damage mechanisms and behaviour of composite materials under low-velocity impacts is of utmost importance to ensure the reliability and safety of composite structures. In this context, it is not surprising that literature presents several strategies to increase impact strength, such as the use of nanoparticles [6], multiaxial mesh fabrics [7], hybrid laminates [8], sandwich composites [9, 10] or simply changing the stacking sequence of the laminates [11].

Since the early 1990s, impact analysis on composite structures has been a subject of study. Thereafter, several numerical research studies have been done using different abstraction scales and applied methods. The finite element (FE) method has been used extensively to develop models of unidirectional composite plates and evaluate various parameters such as material characteristics, impact energy, and geometry. Yet, there are relatively few studies that analyse the impact dynamics on cylindrical shells, particularly when it comes to composites made of woven fabrics. The most relevant studies found in literature regarding low-velocity impact on cylindrical shells, are dedicated to analyse the effect of curvature of the shell on the impact force, displacement (deflection) and contact time [12–15]. The findings of these studies are consistent and reveal that the impact force increases with the increase in curvature, while deflection and contact time decrease. Investigations have also been conducted to determine how thickness affects the impact response of composite laminate plates and shells [16–21]. These studies have shown that increasing the thickness of the laminates leads to notable effects on several impact-related parameters. It was found that increasing the thickness of the composite laminates results in increased stiffness. This higher stiffness imparts the laminates with the ability to withstand higher impact loads. As a result, the laminates exhibit smaller deflections and reduced contact times during impact events. Furthermore, the damage onset and damage evolution were studied in [22], and it was found that for unidirectional composite plates and shells, damage progresses differently. Although the numerical approach utilizing FE models allows the simulation of complicated structures under ostensibly complex external loads and boundary conditions, from the numerical perspective, simulating impact is still a complex task. Moreover, achieving a suitable level of accuracy in a fair amount of time continues to be a challenge [23, 24].

Composite materials experience several different damage modes under im-

*Corresponding author
Email address: lmarques@us.es (L.M. Ferreira)

pact loads such as matrix cracking, delamination, fibre failure and perforation, which can considerably lessen the material's strength and stiffness [25]. It is then crucial to develop credible FE models capable of forecasting these damage modes. Focus is here on fabric-reinforced composite laminate shells with a semicylindrical cross-section. These composites have practical interest for impact-resistant constructions like wind turbine blades or aircraft structures. The built-in continuum damage mechanics model (CDM) for fabric reinforced composites available in ABAQUS [26] and developed by Johnson [27], is employed to model the intralaminar damage, while the interlaminar damage, know as delamination, is modelled using the surface-based cohesive damage model (S-BCM). The two-step homogenization method proposed by Liu et al. [28] is used to predict the laminas' properties from the constituents properties. This study follows the experimental and numerical work previously developed by the authors [29–31]. Firstly, the effect of thickness on the multi-impact response of semicylindrical composite laminated shells with 6-, 9-, and 12-layers was experimentally analysed in [29]. Subsequently, based on the experimental results obtained, a FE model for a single thickness was generated, and in which the physical intralaminar and interlaminar progressive damage models were introduced [30]. This work focused on effect of the FE mesh discretization and mass-scaling on the load history predictions and in evaluating the efficiency and reliability of the numerical model. Afterwards, the influence of interlaminar properties on delamination predictions for a single thickness was studied in [31]. Finally, the present paper represents an expansion of the analysis and validation process to encompass different thicknesses, while striving to comprehend the underlying damage mechanisms at both the intralaminar and interlaminar levels.

Therefore, to summarize, the current work serves as a continuation of the previous numerical investigation and complements the experimental findings. It introduces novel contributions, including the development and validation of FE models capable of investigating the impact dynamics of semicylindrical woven composite laminate shells with different thicknesses. Moreover, the study focuses on predicting and evaluating the intralaminar and interlaminar damage modes, as well as identifying the energy dissipation mechanisms that occur during low-velocity impact events. As far as the authors are aware, these topics in the domain of thin semicylindrical composite shells, are still lacking comprehensive understanding and research.

2. Damage models

Low-velocity impacts on composite laminates can cause fibre failure and matrix cracking (intralaminar damage), as well separation of the interface regions, known as delamination (interlaminar damage) [32, 33]. To model these damage mechanisms in semicylindrical woven composite laminate shells, a CDM at the lamina level to address the intralaminar damage, and a S-BCM at the lamina's interface to account for the interlaminar damage, were implemented. These

damage models are fully described in [26, 34, 35], thus only the main aspects of the CDM and S-BCM will be briefly described in the following subsections.

2.1. Intralaminar damage model

To evaluate the complex damage evolution at the intralaminar level, the built-in constitutive model for fabric reinforced composites available in ABAQUS/Explicit [36], developed by Johnson [27] and based on Ladeveze and Ledantec work [37], was employed. This damage model is applied as a built-in VUMAT user subroutine and accessed by naming the user-defined material with the string "ABQ_PLY_FABRIC" [26]. This VUMAT subroutine is compatible only with plane-stress elements and considers each fabric reinforced lamina as a homogeneous orthotropic elastic material that withstands stiffness reduction due to fibre failure and/or matrix cracking and plastic deformation under shear loading. It uses the maximum stress failure criterion to determine the damage onset of the fibres, and a damage evolution model based on the fracture energies to control the stiffness reduction.

The Hooke's law for a degraded orthotropic material is expressed as,

$$\varepsilon = \begin{bmatrix} \frac{S_1}{(1-d_1)} & S_{12} & 0 \\ S_{21} & \frac{S_2}{(1-d_2)} & 0 \\ 0 & 0 & \frac{S_6}{(1-d_{12})} \end{bmatrix} \sigma \tag{1}$$

where S_{ij} are the components of the compliance matrix of the undamaged orthotropic material, σ is the nominal Cauchy stress tensor, ε is the elastic strain tensor, and d_1, d_2 and d_{12} are the damage coefficients. Notice that the damage coefficients d_1 and d_2 are associated with fibre fracture along directions 1 and 2, respectively, and d_{12} is associated with the matrix micro-cracking due to shear deformation.

As mentioned before, the CDM uses the maximum stress criterion to determine the damage onset of the fibres, and to simulate the two failure modes (fibre tension and fibre compression). Therefore, the elastic domain, at any given time, is calculated in terms of the damage activation functions, F_α, as

$$F_\alpha = \frac{\tilde{\sigma}_\alpha}{X_\alpha} - r_\alpha \leq 0 \text{ with } \alpha = 1\pm, 2\pm, 12 \tag{2}$$

where $\tilde{\sigma}_\alpha$ and X_α are the tensile/compressive/shear effective stresses and strengths, respectively, and r_α are the damage thresholds, which are initially defined with a value of 1. After reaching the damage onset, that is, when $\frac{\tilde{\sigma}_\alpha}{X_\alpha} = 1$, the evolution the damage coefficients, d_1 and d_2, associated with the tensile and compressive loading, are obtained using equations 3 and 4, while the damage coefficient d_{12} associated with shear loading, is obtained by equation 5,

$$d_{1,2} = 1 - \frac{1}{r_{1,2}} e^{-A_{1,2}(r_{1,2}-1)} \tag{3}$$

$$A_{1,2} = \frac{2 g_0^{1,2} L_{ch}}{G_f^{1,2} - g_0^{1,2} L_{ch}} \quad with \; g_0^{1,2} = \frac{X_{1,2}^2}{2E_{1,2}} \tag{4}$$

$$d_{12} = min\left[\alpha_{12}\ln\left(r_{12}\right),\ d_{12}^{max}\right] \tag{5}$$

where $r_{1,2}$ and r_{12} correspond to the damage thresholds for the tensile/compressive and shear loading, respectively, $G_f^{1,2}$ to the fracture energies per unit area, $g_0^{1,2}$ to the elastic energy density at the damage onset, and L_{ch} to the characteristic length of the element. The shear damage parameter α_{12} is obtained through a calibration procedure detailed in [26].

At the intralaminar level, the shear damage response is driven by the matrix's nonlinear behavior caused by the matrix microcracking, and it involves both stiffness loss and plasticity. The yield and hardening functions represented in equations 6 and 7, respectively, are used by the VUMAT subroutine to define the plasticity response of the matrix,

$$F_{pl} = |\tilde{\sigma}_{12}| - \tilde{\sigma}_0(\bar{\varepsilon}^{pl}) \leq 0 \tag{6}$$

$$\tilde{\sigma}_0(\ \bar{\varepsilon}^{pl}) = \tilde{\sigma}_{y0} + C(\ \bar{\varepsilon}^{pl})^p \tag{7}$$

where $\tilde{\sigma}_{12}$ is the effective shear stress, $\tilde{\sigma}_{y0}$ is the initial effective shear stress, and $\bar{\varepsilon}^{pl}$ is plastic strain due shear deformation. The hardening function's coefficient and power term are denoted by C and the superscript p, respectively.

To be able to validate the numerical models based on the experimental evidence presented in [29], the stiffness properties of the woven fabric composite laminas were estimated from the constituents' properties of the tested specimens, using the two-step homogenization methodology presented by Liu et al. [28]. The obtained elastic properties are consistent with those reported in literature for plain weave E-glass woven fabric composites [38–40]. This multiscale approach involves first estimating the effective properties of the tows from the fibre and matrix properties and then predicting the lamina properties from the properties of the tows and the matrix. This methodology was implemented using the software TexGen4SC [41, 42]. Each lamina is composed of a polyester resin matrix (AROPOL FS 1963 with MEKP-50 hardener) reinforced with a bi-axial E-glass plain weave fabric (EC9 68×2). The lamina's stiffness properties were estimated from the elastic constants extracted from [43–46]. The remaining properties and coefficients required to implement the VUMAT subroutine, such as the strength properties, fracture toughness and shear plasticity, were taken from literature [38, 47–51]. The lamina's intralaminar properties are shown in Table 1. Notice that a good agreement between the experimental results and the numerical predictions was attained in previous work developed by the authors, and in which the same properties and coefficients were employed [30, 31].

The transverse shear stiffness of the laminas must be defined for the VUMAT subroutine [26] because it cannot be calculated by ABAQUS/Explicit [36] for composite shell elements. Considering that each lamina can be thought of as a homogeneous shell with orthotropic elastic properties, equations 8 were used to calculate the transverse shear stiffness,

Table 1: Intralaminar properties defined for each lamina [30].

Property	Symbol	Units	Value
Density	ρ	kg/m^3	1900
Stiffness properties	$E_1^{+,-} = E_2^{+,-}$	GPa	21.9
	E_3	GPa	8.6
	G_{12}	GPa	3.4
	G_{13}	GPa	2.4
	ν_{12}	-	0.14
Strength properties	$X_1^+ = X_2^+$	MPa	250
	$X_1^- = X_2^-$	MPa	200
	X_{12}	MPa	40
Fracture toughness	$G_f^{1,2}$	J/m^2	4500
Shear plasticity	d_{12}^{max}	-	1
	$\tilde{\sigma}_{y0}$	MPa	25
	C	-	800
	p	-	0.552

$$k_1^{ts} = \frac{5}{6} G_{13} t, \quad k_2^{ts} = \frac{5}{6} G_{23} t, \quad k_{12}^{ts} = 0 \tag{8}$$

where G_{13} and G_{23} are the out-of-plane shear moduli of the lamina, t is the thickness of the lamina, and 5/6 is a shear correction coefficient that is obtained by comparing the transverse shear energy to that for an 3D structure in pure bending, as suggested in [36]. Considering the out-of-plane shear moduli calculated by the homogenization process, the following values were used in the definition of the intralaminar properties: $k_1^{ts} = k_2^{ts} = 3.5 \times 10^5$ N/m and $k_{12}^{ts} = 0$.

2.2. Interlaminar damage model

To account for the interlaminar damage, i.e. delamination, the bond between the laminas of the composite laminate was modelled using a S-BCM. This model is primarily intended for negligible small interface thicknesses and offers very similar capabilities to cohesive elements. The cohesive behaviour is defined as a surface interaction property, and identically to the cohesive elements it is governed by a traction-separation constitutive model. Hence, the interlaminar fracture behaviour (delamination) is defined as a constitutive relation between the traction τ and the separation δ, see Fig. 1.

The initial linear response until the damage onset it reached is controlled by the value defined for the normal k_n and tangential k_s, k_t cohesive stiffnesses. These parameters influence the performance of the FE model and for which there are different approaches available in literature to obtain its value [52–55]. For instance, Daudeville et al. [52] determined the cohesive stiffness as a function

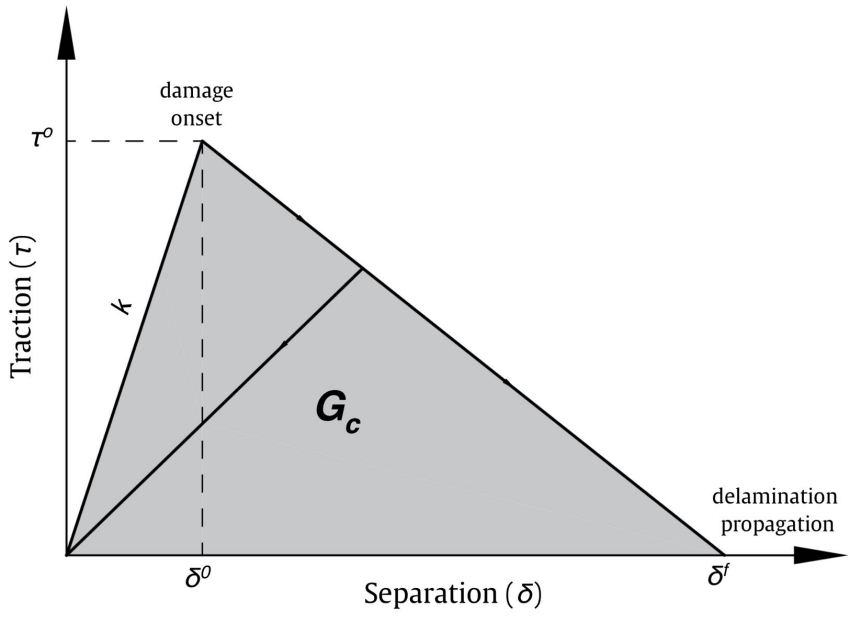

Figure 1: Bilinear traction-separation response of the cohesive surface.

of the interface's thickness and the elastic modulus of the resin-rich layer, while Zou et al. [53] suggested the use of interface stiffness values between 10^5 and 10^7 times the interface strength divided by length unit. Another approach was presented by Turon et al. [55], in which the interface stiffness is calculated as function of the elastic properties of the laminate. The cohesive stiffness in this study is set at 10^6 N/mm^3, as suggested by Camanho et al. [54]. Also, it is considered that its value is the same for all directions, that is, $k_n = k_s = k_t$, as used in [30, 31, 55–57] with satisfactory results. It is noteworthy that considering high values for the cohesive stiffness potentially leads to convergence problems, on the other hand, the use of low values may affect the global stiffness and thus compromise the validation of the FE model [56].

The following stress-based quadratic failure criterion was employed to predict the damage initiation,

$$\left(\frac{\langle\ \tau_n\rangle}{\tau_n^0}\right)^2 + \left(\frac{\tau_s}{\tau_s^0}\right)^2 + \left(\frac{\tau_t}{\tau_t^0}\right)^2 = 1 \tag{9}$$

where τ_n, τ_s and τ_t represent the interface normal and shear contact stresses, and τ_n^0, τ_s^0 and τ_t^0 represent the corresponding interface strengths. The Macaulay brackets $\langle\ \rangle$ indicate that the compressive stress doesn't contribute to damage. The following interlaminar strengths were used in the S-BCM: $\tau_n^0 = 15$ MPa and $\tau_s^0 = \tau_t^0 = 30$ MPa [30]. Once the onset of damage is reached, that is, when the quadratic interaction function of the stress ratios reaches 1, the cohe-

sive stiffness is degraded. Equation 10 represents the softening response of the cohesive surface where d is the damage coefficient.

$$\tau_i = (1-d)\, k_i \delta_i \quad with\ i = n, s, t \tag{10}$$

In this model, the damage evolution is controlled by the energy dissipated during the damage process G_c, which corresponds to the area below the $\tau - \delta$ curve represented in Fig. 1. This fracture energy establishes the nature of the evolution of the damage coefficients between de onset of damage and final failure. The fracture energy G_c is calculated by the Benzeggagh and Kenane (B-K) criterion [35] under mixed-mode loading using equation 11.

$$G_c = G_{Ic} + (G_{IIc} + G_{Ic}) \left(\frac{G_{II} + G_{III}}{G_I + G_{II} + G_{III}} \right)^{\eta} \tag{11}$$

Where G_I, G_{II} and G_{III} are the strain energy release rates under mode I, II and III respectively, G_{Ic} and G_{IIc} represent the critical strain energy release rates (assuming that $G_{IIc} = G_{IIIc}$) and η represents an interaction parameter. In this study, the following values were employed in the S-BCM: $G_{Ic} = 300$ J/m^2, $G_{IIc} = G_{IIIc} = 600$ J/m^2 and $\eta = 1.45$ [30].

3. Finite element models

In this section, the FE models used in the numerical simulations of low-velocity impact tests are described. These models were generated based on the experimental tests carried out by the authors [29], and the numerical study conducted in [30] using ABAQUS/Explicit FE code [36]. In this way, and to properly simulate the low-velocity impact response of the specimens, the following parameters had to be correctly defined: geometric parameters of the specimens and impactor, mesh discretization, boundary conditions, impact energy, intralaminar and interlaminar material properties, and contact properties between all modelled parts (impactor/lamina, lamina/lamina and lamina/supports).

3.1. Geometric parameters and boundary conditions

The geometric parameters of the 6-, 9- and 12-layer specimens tested in [29] were taken into account when creating the FE models. These specimens have a semicircular cross-section with an internal radius of 50 mm and a length of 100 mm, as shown in Fig. 2(a) Three different thicknesses were considered: 1.1 mm, 1.6 mm, and 2.1 mm, corresponding to the 6-, 9-, and 12-layer laminates, respectively.

Two fixed rigid body supports (a lateral and a bottom support) were incorporated into the FE models in order to replicate the supports used in the experiments, in which the bottom straight faces of the laminate (face parallel to the xz-plane in Fig. 2(b) were simply supported and there were lateral vertical supports that constrained the displacement along the x-direction. Taking advantage of the model's geometric symmetries to reduce the computational cost of the numerical studies, only one-fourth of the semicylindrical composite

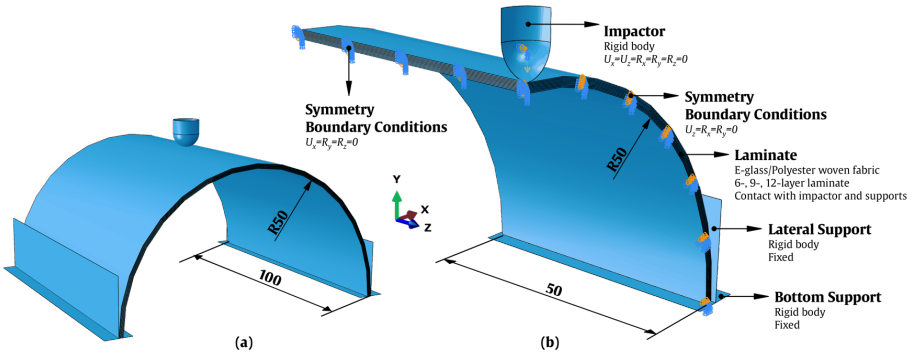

Figure 2: FE model with geometric parameters and boundary conditions: (a) Complete FE model; (b) One-fourth of the FE model.

laminate was generated. Thus, the face parallel to the yz-plane, and one of the faces parallel to the xy-plane, both were added symmetry boundary conditions, as detailed in Fig. 2(b).

To be able to perform the numerical correlation with the results obtained in [29], the impactor was modelled with a hemispherical head of 10 mm in diameter and a lumped mass fixed on a reference point at its centre of mass equivalent to the experiments. The rotations of the impactor were constrained, and only the displacements along the y-direction were allowed. An impact velocity of 1.9 m/s was considered in the numerical analysis, which corresponds to the impact energy of 5 J used in [29]. This impact energy/impact velocity was selected to promote visible damage, but without perforation of the specimens. More details about the experimental procedure and the drop weight impact machine can be found in [29, 58].

3.2. Mesh strategy and element types

The parts that comprise the FE models, laminas, impactor and supports, were generated with distinct strategies. Continuum shell elements (SC8R) with reduced integration and stiffness hourglass formulation were used to discretize each lamina. These continuum shell elements are suitable for impact simulations and its computational cost is lower when compared to solid elements [59, 60]. The material orientations along the semicircular cross-section were taken into consideration when defining the local coordinate systems. The element deletion option was disabled because no penetration was observed for a single impact on the experimentally tested specimens [29].

The impactor was modelled with discrete rigid elements (R3D4) with the same FE mesh size of the laminas, as shown in Fig. 3. The supports were modelled as analytical rigid bodies, thus no element and mesh definitions were required. Considering that the lamina's interface thickness is negligible, it was modelled with cohesive surfaces, thus bypassing the need for element definition.

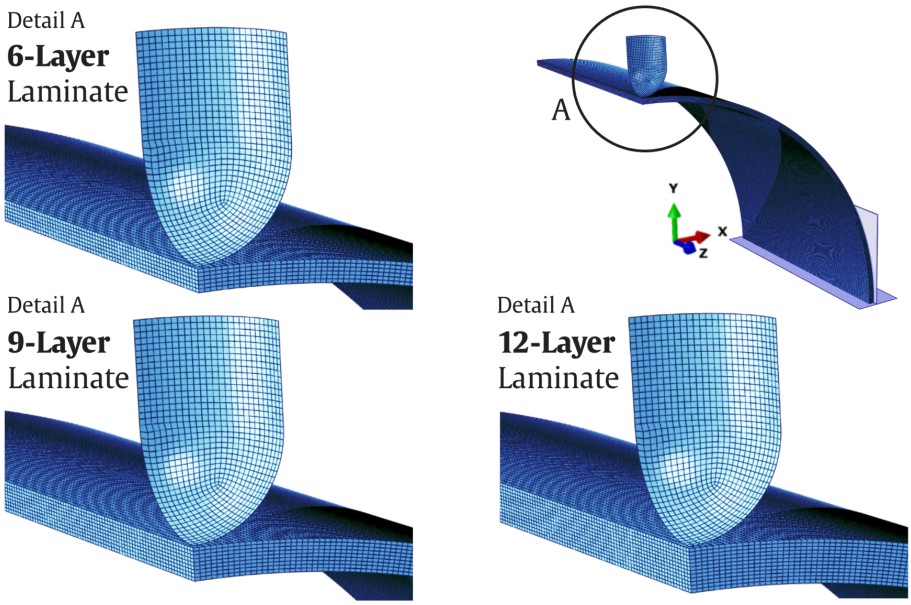

Figure 3: Detailed views of the FE mesh used in the numerical models.

A previous parametric study was conducted by the authors to optimize the aspect ratio of the elements of the FE mesh and to find a balance between the computational cost of the solution and the accurate computation of the fracture energy G_c in the interlaminar damage model, which results in delamination [30]. The study revealed a good agreement between the numerical predictions and the experimental evidence for an element's characteristic length of $L_{ch} = 0.3$ mm. Notice that this value was obtained using the approach presented by Turon et al. [55] for orthotropic composite materials. Consequently, in this study, all the FE models were generated with identical mesh size. Moreover, an uniform FE mesh was taken into consideration in order to produce an accurate prediction of damage throughout the model, because it was observed in [29] that damage in the semicylindrical woven composites may be not limited to the impact zone, particularly on the laminates with small thickness. Notice that the 6-, 9-, and 12-layer laminates were created by assembling identical models of each lamina. Detailed views of the FE mesh employed in each of the generated FE models is shown in Fig. 3.

The 12-layer FE model used in this study, for instance, contains more than 500,000 elements and 1,000,000 nodes. Therefore, a semi-automatic mass scaling was uniformly applied to the entire model to shorten the computing time for the solutions. All studies had a target time increment of 10^{-7}s, which resulted in mass increases of 1.2%, 1.8%, and 2.4% for the 6-, 9-, and 12-layer FE models, respectively. The effect of mass-scaling on the simulations was analysed in [30] and it was found that the accuracy of the dynamic response is not compromised with the defined target time increment, while reducing the computation cost of

the solution by about 50%.

3.3. Contact definition

The penalty enforcement contact method from ABAQUS/Explicit [36] was used to simulate the surface-to-surface contacts that arise between the composite laminate, the metal impactor, and the metal supports [61]. This contact formulation was also defined at the interface of the laminas that experience friction once fully delaminated. The FE model was defined so that all the surfaces that encounter another experience friction. In this study, the friction coefficient values μ for the metal-composite contacts and fully damaged interfaces were taken from literature [62, 63]. Therefore, a value of $\mu = 0.3$ was specified for the contact between the metal hemispherical head of the impactor and the top surface of the composite laminate, and a value of $\mu = 0.7$ for the contact between the metal surfaces of the supports and the composite laminate surfaces. A value of $\mu = 0.5$ was thought of for the laminas' interface.

4. Numerical results

In this section, the numerical predictions obtained with the 6-, 9- and 12-layer FE models are compared with the experimental findings presented in [29]. The maximum impact force, maximum displacement, and impact bending stiffness (IBS) values are shown and discussed, together with the force-time, force-displacement, and energy-time curves. The deformation histories and the predicted intralaminar and interlaminar damage are also represented and contrasted with the experimental evidence.

4.1. Load histories

Representative experimental force-time and force-displacement curves for the 6-, 9- and 12-layer composite laminates are plotted along with the numerical predictions in Figs. 4 and 5, respectively. Overall, for all thicknesses, a satisfactory numerical-experimental correlation can be observed for the loading stage. For the unloading stage, on the other hand, the simulation results slightly differ from the results of the tested specimens. This can be justified by the fact that the simulations do not account for the permanent indentation that in practice occurs on the specimens after the impact. As a result, the simulated specimens resume their original shape after unloading.

It is possible to derive from the data in Table 2 that the maximum impact force that the specimens can withstand is correctly predicted by the 6- and 9-layer FE models, and even though the results of the simulations are slightly overestimated, they are within the bounds of the experimental data. The 12-layer FE model, on the other hand, underestimates the maximum force by 11.5%, falling outside the measured results. Notice that the percentage error in Table 2, compares the numerical with the averaged experimental values. The effect of thickness on the numerical and actual averaged maximum force results is shown

Table 2: Comparison between numerical and experimental [29] results for the 6-, 9- and 12-layer composite laminates (maximum force, maximum displacement, contact time and IBS).

Laminate	Maximum Force			Maximum Displacement			Contact time			IBS		
	Num. (N)	Exp. (N)	Error (%)	Num. (N)	Exp. (N)	Error (%)	Num. (N)	Exp. (N)	Error (%)	Num. (N/mm)	Exp. (N/mm)	Error (%)
6-Layer	518	487±41	6.1	17.2	16.6±0.8	3.4	38	35.9±2.3	5.5	27	31.3±5	15.9
9-Layer	797	757±50	5	11.5	11.2±1.3	2.7	23	20.6±3.1	10.4	54	60.8±9	12.6
12-Layer	1068	1191±45	11.5	7	6.7±1.5	4.6	13.5	12.2±1.9	9.6	128	122.6±9	4.2

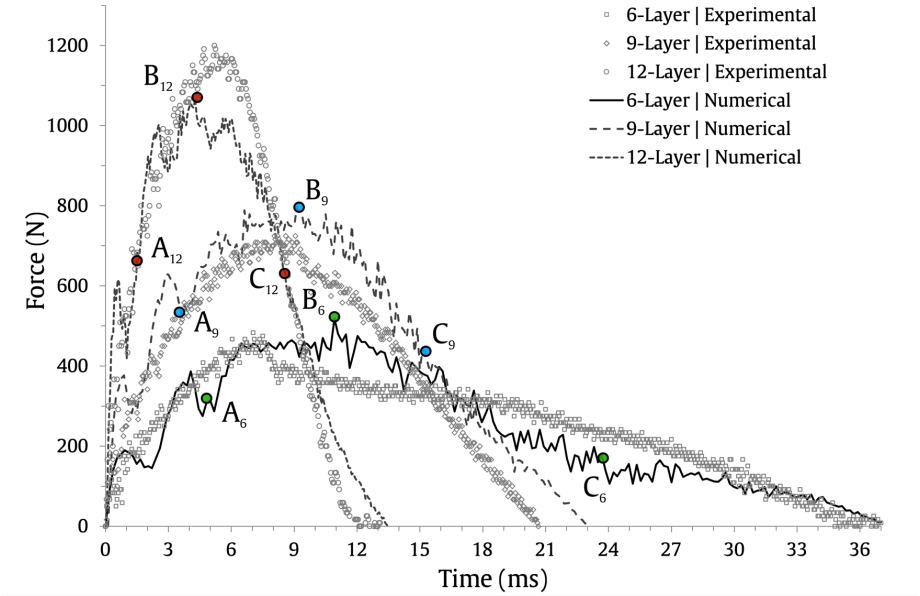

Figure 4: Numerical and experimental [29] force-time results for 6-, 9-, and 12-layer laminates.

in Fig. 6, where the scatter bands represent the maximum and minimum experimental values. It is possible to verify from the represented trend lines (dashed lines), that the FE models properly simulate the linear response observed in the experiments, increasing with the increase in thickness. The maximum displacement is well predicted for all the studied thicknesses, as shown in Table 2. Its values are marginally overestimated, with errors ranging from 2.7% for the 9-layer laminate, to 4.6% for the 12-layer laminate. The effect thickness on the numerical and averaged experimental maximum displacement results is shown in Fig. 7. Again, the FE models properly replicate the linear response found in the experiments, but this time decreasing with the increase in thickness. Finally, Table 2 shows that the predicted contact time fall within the range of the experimental results, presenting errors ranging from 5.5% to 10.4%.

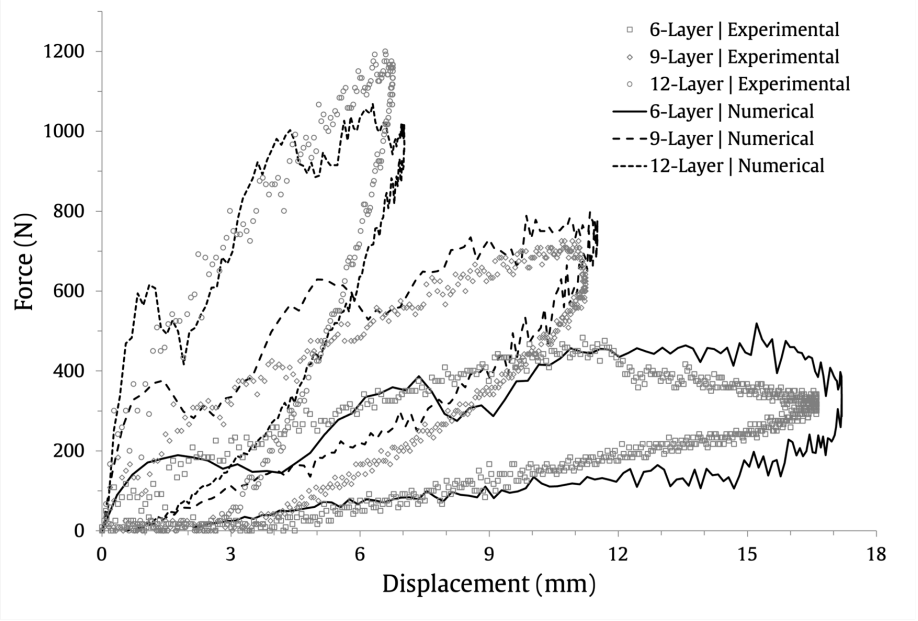

Figure 5: Numerical and experimental [29] force-displacement results for 6-, 9-, and 12-layer laminates.

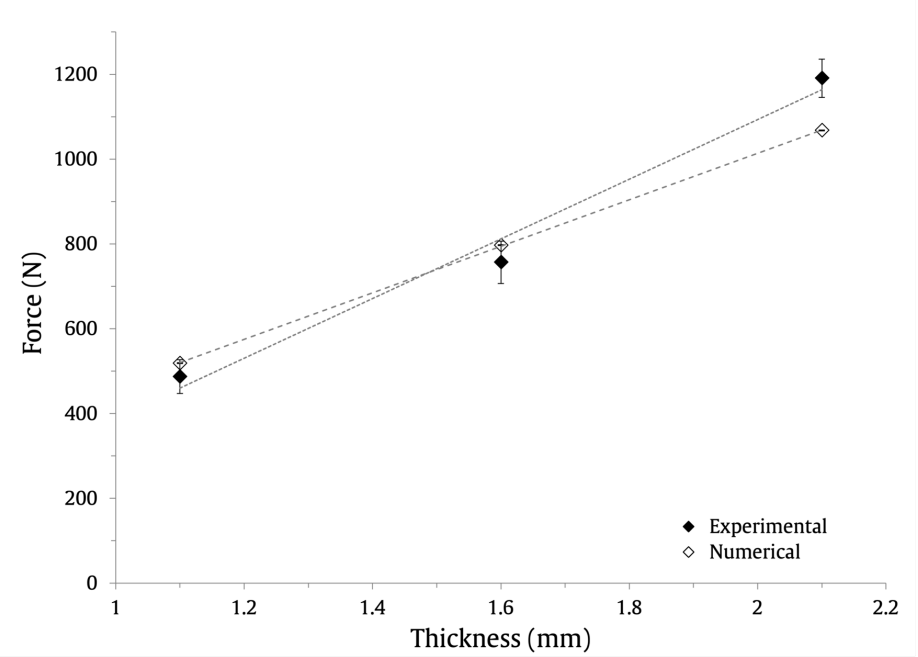

Figure 6: Effect of thickness on the numerical and experimental [29] maximum force results.

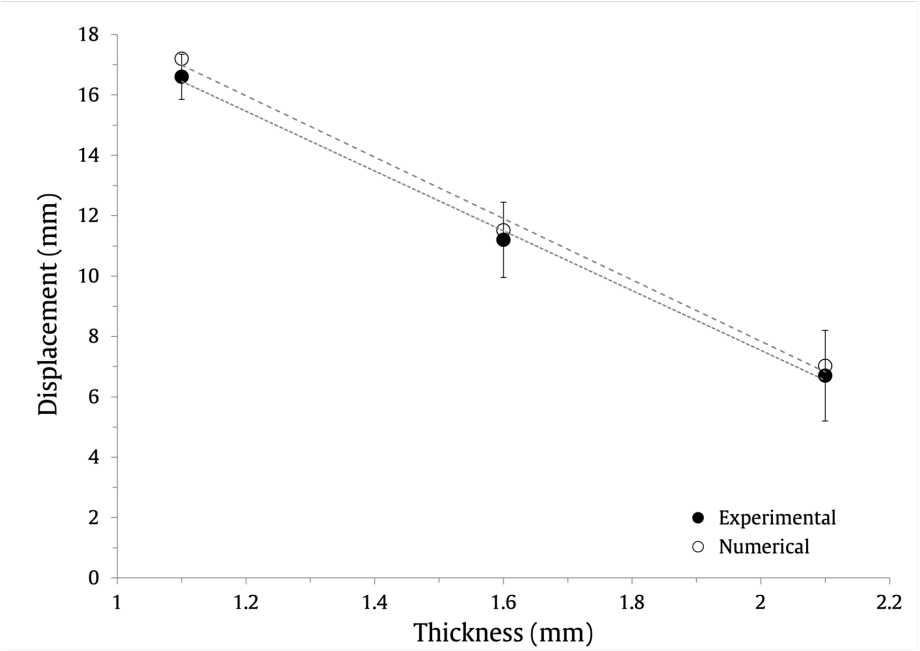

Figure 7: Effect of thickness on the numerical and experimental [29] maximum displacement results.

4.2. Deformation histories

The deformation histories of the 6-, 9- and 12-layer composite laminates at different step times are shown in Fig. 8. The selected time steps for analysis are represented in Fig. 4, denoted as A_i, B_i and C_i, which correspond to the following contact times: A_i to half of the peak force time; B_i to the peak force time; C_i to half of the time between the peak force and the total contact time. Here, the subscript $i = 6, 9, 12$, identifies the configuration of the laminate.

A notable trend can be observed wherein an increase in thickness results in a corresponding increase in the stiffness of the composite laminate. Among the laminates studied, the 6-layer laminate exhibits the highest degree of deformation, followed by the 9-layer and 12-layer laminates. As anticipated, the deformation steadily intensifies until it reaches the peak force, at which point the impactor rebounds and the specimen commences its elastic recovery.

4.3. Impact bending stiffness

The studies developed by Liu [64] and David-West et al. [65] suggest that the impact bending stiffness is an important parameter to evaluate the damage resistance of a composite, in particular delaminations. According to these authors, the slope of the ascending branch of the load-displacement curve defines the IBS, because the plate is under bending at the beginning of the impact

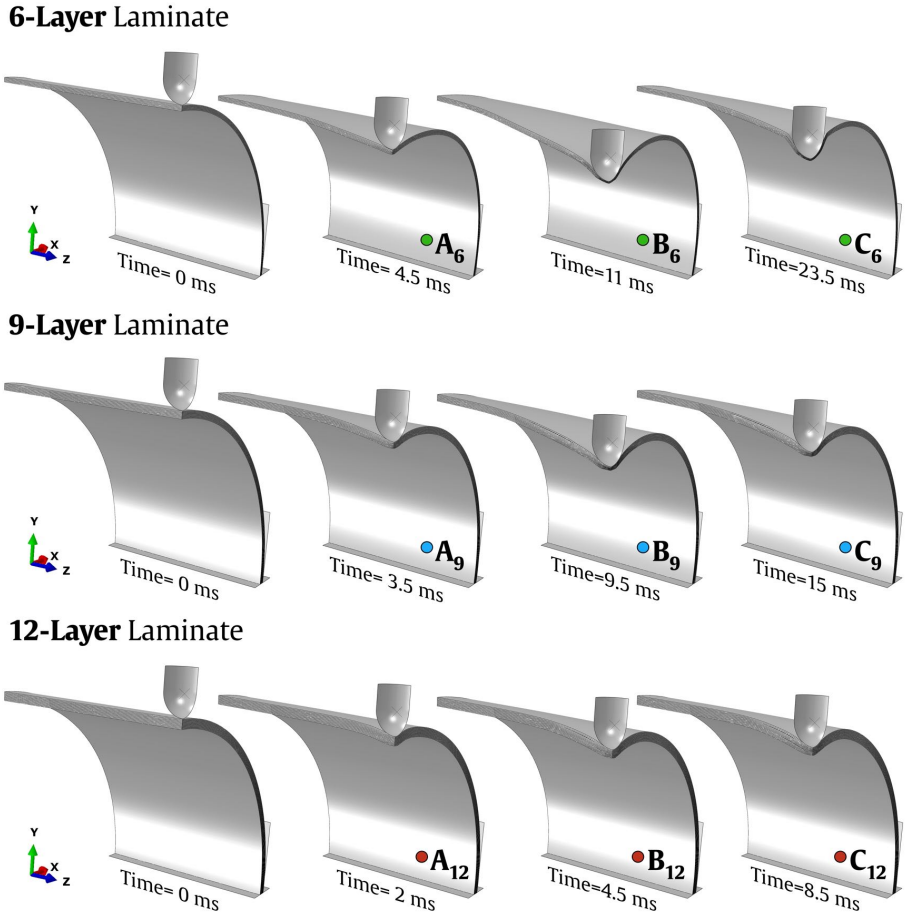

Figure 8: Deformation histories for the 6-, 9- and 12-layer composite laminates.

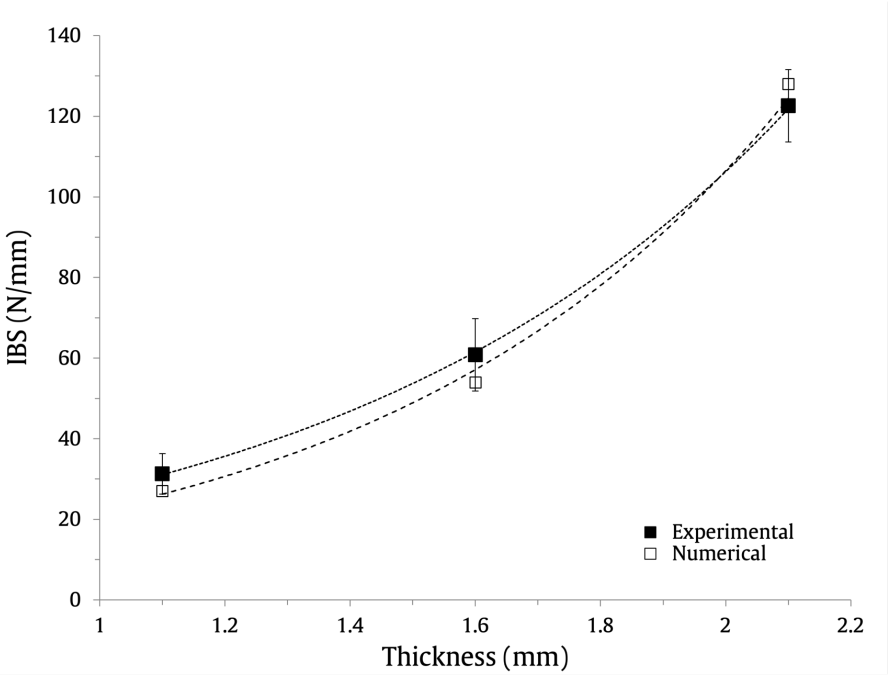

Figure 9: Effect of thickness on the numerical and experimental [29] IBS results.

regime [65]. In this study, the IBS is calculated from the experimental and numerical curves depicted in Fig. 5, and Table 2 presents and compares the values obtained. It should be noted that the IBS predictions for the 6-layer FE model had the largest percentage of error. This is most likely because damage begins to appear at slightly different loads than simulated. Actually, until reaching the peak force, the experiments shown a smoother damage growth than the simulations. This difference in the initial behaviour can be attributed to the use of the semi-automatic mass scaling technique in the numerical models [30]. Nevertheless, all the predicted IBS values are within the limits of the experimental evidence. The evolution of the IBS with thickness is shown in Fig. 9. The figure outlines the FE models capability to accurately reproduce the 2^{nd} order polynomial curve followed by the experiments, and which are represented by the plotted trend lines.

4.4. Damage

The numerical predictions for the intralaminar damage (output variables SDV1 to SDV5) and the interlaminar damage (output variable CSDMG>0.6) were overlapped to allow a complete representation of the damage severity for the different laminate thicknesses, see Figs. 10, 11 and 12. Notice that the output identifier CSDMG, represents the scalar stiffness degradation for cohesive surfaces, and measures delamination after damage initiation. When it reaches

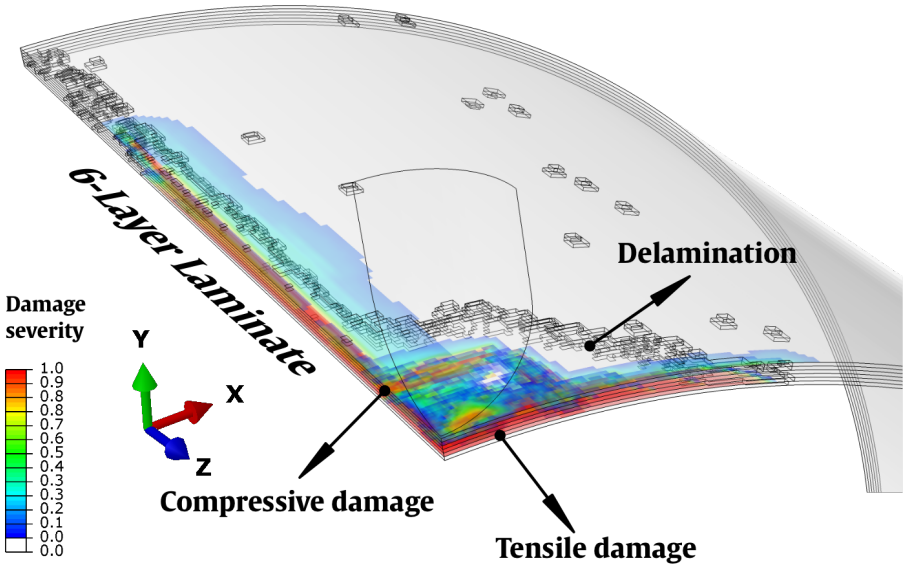

Figure 10: Numerically predicted tensile and compressive damage along the fibre directions and delaminated area for the 6-layer laminate.

the value of 1, the interface is considered to be fully delaminated. Moreover, the CDM for fabric reinforced composites used in this study does not differentiate between fibre and matrix damage at the intralaminar level, it includes only the outputs variables of tensile/compressive damage along the fibre directions and the shear damage. Therefore, it limits a more detailed identification of the damage modes at the intralaminar level.

The simulations show that laminate's thickness affects how severe the damage is. The 6-layer FE model sustained damage commencing at the point of impact and extending the full length of the shell. The 9-layer FE model predicted a less severe damage but quite similar to the one obtained with the thinner laminate. On the other hand, damage is restricted to the impact location for the 12-layer FE model. This response can be explained by the fact that more interfaces are available to dissipate the impact energy as thickness increases and consequently, there is less energy available to increase damage. These results are consistent with the experimental findings, which showed that the damaged severity increases with decreasing thickness [29]. Moreover, it correlates with the larger displacements observed in thinner laminates, see Fig. 5.

Moreover, it is also possible to appreciate in Figs. 10 to 12, that regardless of the thickness, the damaged incurred in the bottom layers of the shell is more severe in comparison to the top layers. It is known that during a low-velocity impact event, the bottom layers of the shell, located opposite to the impact side, experience tensile stresses resulting in material (fibre and matrix) elongation. Conversely, the top layer of the shell, which comes into direct contact

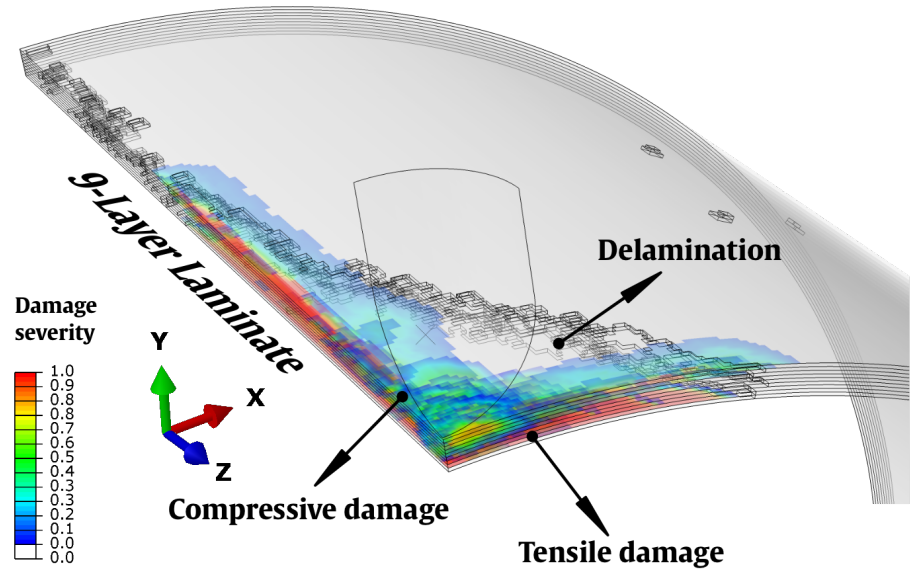

Figure 11: Numerically predicted tensile and compressive damage along the fibre directions and delaminated area for the 9-layer laminate.

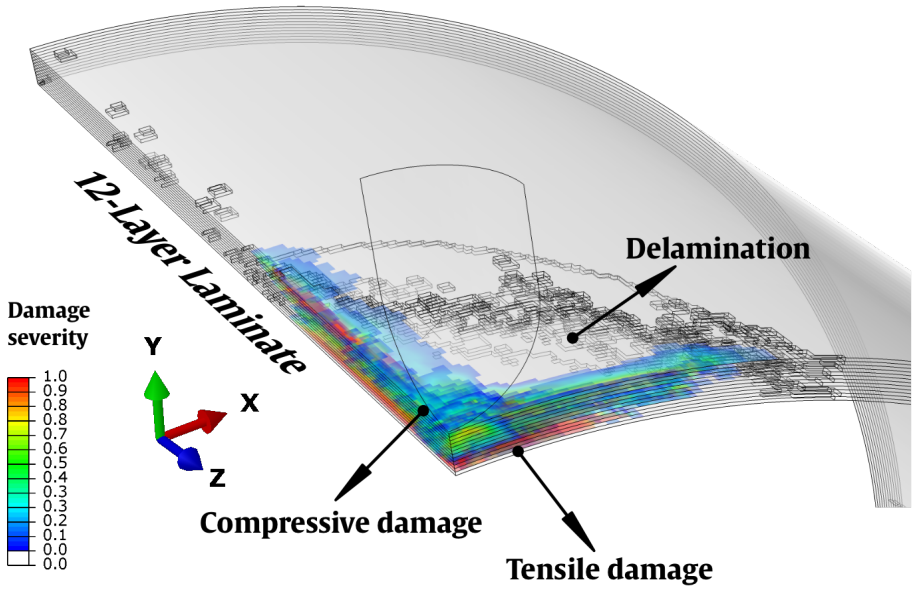

Figure 12: Numerically predicted tensile and compressive damage along the fibre directions and delaminated area for the 12-layer laminate.

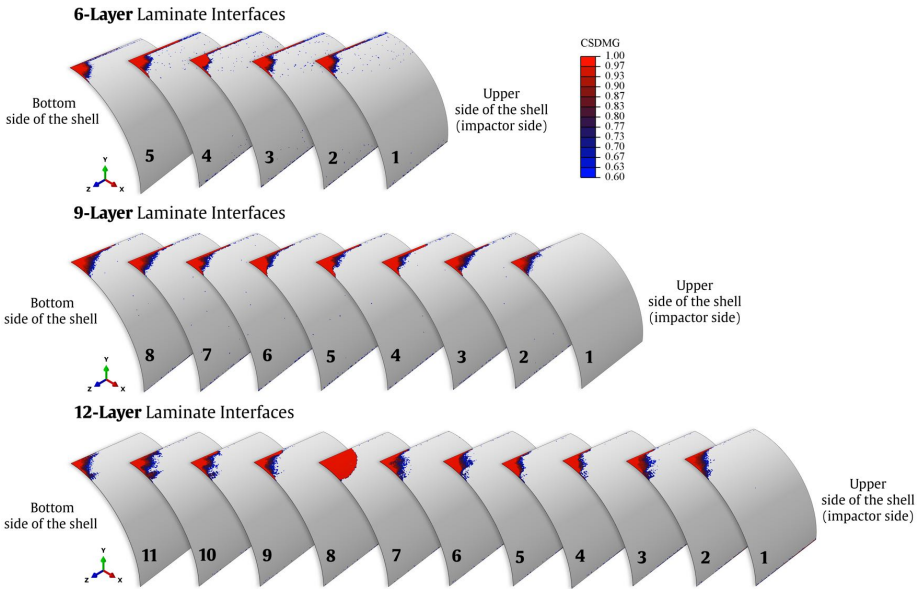

Figure 13: Delamination predictions along the different interfaces of the 6-, 9-, and 12-layer composite laminates.

with the impactor, experiences compression forces. These compression forces induce localized deformation in the impacted region which undergoes plastic deformation and compression. Although the CDM does not provide specific identification of the various damage modes, the numerical predictions suggest that at the intralaminar level, the most prominent damage mechanisms are fibre breakage and/or matrix cracking. These damage modes are closely associated with the tensile stresses developed in the bottom layers during the impact event.

The delamination areas predicted for each interface of the laminates are illustrated in Fig. 13. Once again, it is evident that delamination primarily occurs within the impact region. However, as previously observed, the delamination in the 6- and 9-layer laminates propagates along the length of the shell. Regarding the interfaces, it is noteworthy that for the same laminate thickness, they generally exhibit similar delamination areas in terms of size and severity. However, there is an exception observed for interface 7 of the 12-layer laminate. This particular interface is located approximately in the middle of the laminate's thickness, between layer 7 and layer 8. The predicted delamination region for this interface is slightly larger and more severe compared to the other interfaces. Nevertheless, the overall results have a good correlation with the experimental evidence presented in Fig. 14.

The predicted impact footprints, resulting from the overlapping of the intralaminar and interlaminar damage modes are compared with the actual impact footprints obtained experimentally, in Fig. 14. Notice that the damage on the tested specimens was captured through photography using intense backlight,

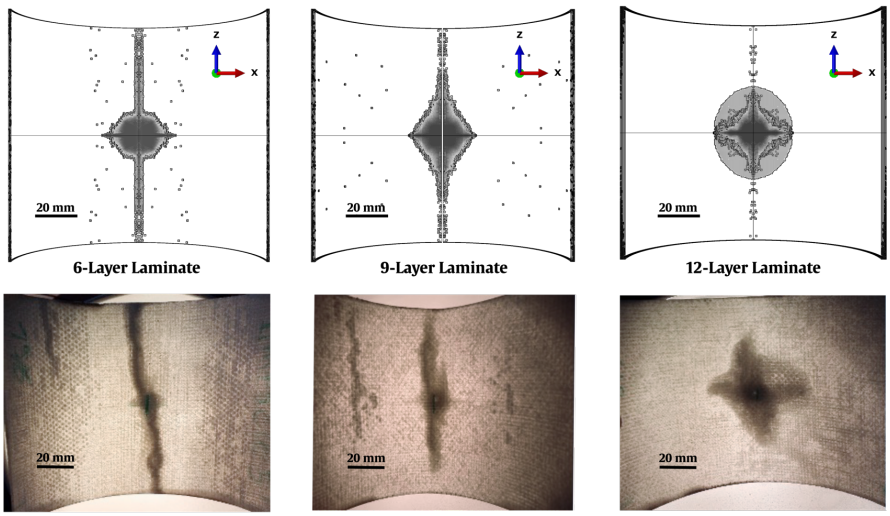

Figure 14: Numerical and experimental [29] impact footprints for the 6-, 9- and 12-layer composite laminates.

taking advantage of the translucent characteristic of the laminates. Despite the limitations on the accuracy of the non-destructive testing technique employed to assess the damage extension, the projected damage areas are generally well predicted by the FE models. The uniform FE mesh size used, contributed for the correct predictions of the damaged areas that can be seen along the length of the laminates. However, it should be noted that they tend to be slightly overestimated around the impact location. The scattered points that can be appreciated in the simulations of the 6- and 9-layer laminates outside the concentrated damaged areas, correspond to isolated nodes which have experienced delamination.

4.5. Energy histories

In the loading stage of a low-velocity impact test, a sizeable portion of the kinetic energy that is transferred from the impactor to the laminate is converted into elastic energy. The remaining energy is dissipated owing to friction and to the different failure modes that occur at the intralaminar and interlaminar levels. The elastic energy that the specimen stores is released during the unloading stage, causing the impactor to rebound. As the impactor loses contact with the specimen, the energy stabilizes [66, 67]. Since in the experimental setup the impactor's mass and the drop height remained consistent across different thickness variations, the peak values observed on the energy-time curves remained identical. This behaviour can be appreciated in the energy histories of the 6-, 9- and 12-layer laminates shown in Fig. 15. Overall, a good numerical-experimental correlation can be appreciated. Notice that the numerical predicted impact energy curves for the 6- and 9-layer laminates present a rugged behaviour during

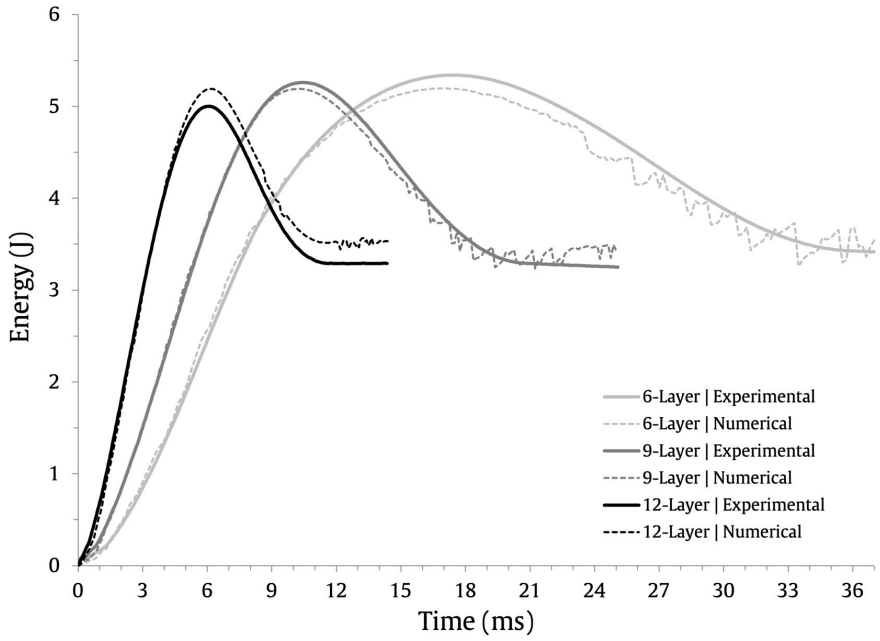

Figure 15: Effect of thickness on the numerical and experimental [29] energy-time results.

the unloading stage, which is due to the vibrations of the FE model. On the other hand, given its higher stiffness, the 12-layer laminate presents a smoother behaviour.

The validation of simulations of the energy and load histories, along with the well predicted damage areas, opens the possibility of identifying the amount of energy that is dissipated through intralaminar damage, delamination and friction. The experimentally measured impact energy converted from the impactor, and the numerical predictions for the impact energy and the subsequent dissipated energy forms obtained with 6-, 9- and 12-layers FE models, are shown in Figs. 16, 17 and 18, respectively.

Regardless of the thickness under consideration, the intralaminar damage outweighs the other energy dissipation forms by about 5 times, confirming that it is the primary damage mode. The energy dissipation due to delamination and friction is negligible, however, a slight increase as thickness increases can be observed. The larger number of interfaces may explain this behaviour. Moreover, the high interlaminar fracture toughness and low in-plane strength of the woven fabric composites may justify the propensity for intralaminar damage propagation rather than delamination.

The total transferred energy curve's peak, which corresponds to the instance of maximum displacement, is correctly predicted, and the energy balance is accurately reproduced. It is noteworthy to mention that the total energy (output ETOTAL), remains stable, which indicates a correct definition of the step time

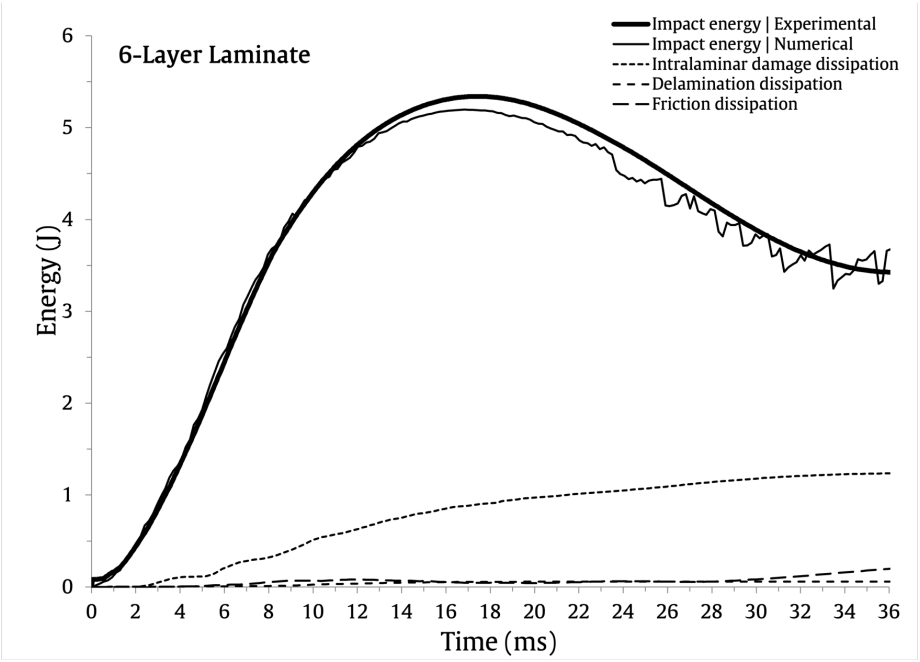

Figure 16: Numerical and experimental [29] energy history for the 6-layer laminate.

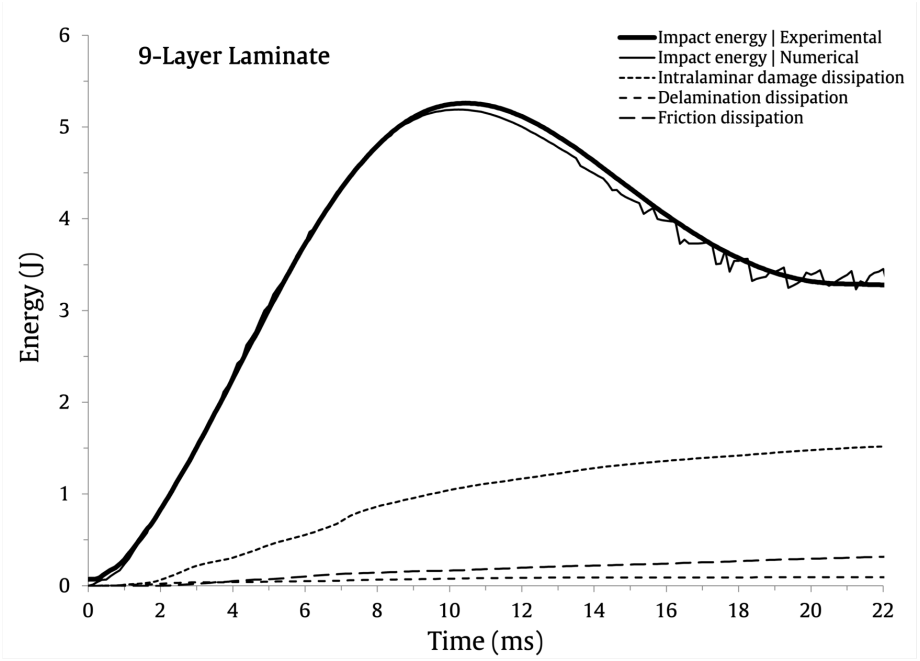

Figure 17: Numerical and experimental [29] energy history for the 9-layer laminate.

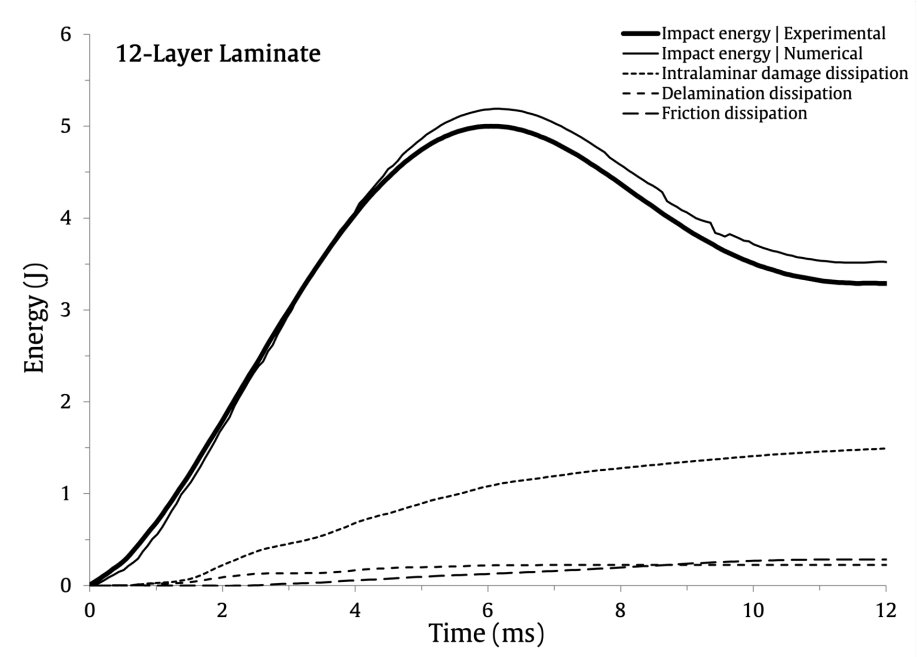

Figure 18: Numerical and experimental [29] energy history for the 12-layer laminate.

increments. Also, the external energy (ALLAE output), is a small fraction of the internal energy (ALLIE output), meaning the hourglass control method is adequate.

5. Conclusions

The intralaminar and interlaminar damage and the impact response of thin semicylindrical woven composite laminate shells under low-velocity impact loads was simulated using the finite element method, with particular focus on evaluating the effect of thickness. The numerical predictions were compared with the findings of the previous experimental work conducted by the authors.

The results obtained in this study, demonstrate that the low-velocity impact response of thin semicylindrical woven composite laminate shells can be reliably simulated using the explicit FE method together with a CDM, to account for intralaminar damage, and a S-BCM, to account for interlaminar damage. The numerical models were able to satisfactory predict the load histories, as well as the maximum impact force, maximum displacement, contact time, and IBS. For example, the simulations were able to reproduce the experimental linear response of the maximum impact force and maximum displacement to the thickness variation, as well as the 2^{nd} order polynomial curve of the IBS followed by the experiments.

Additionally, the predicted impact footprints that resulted from the overlapping of the intralaminar and interlaminar damage modes, showed a good agreement with the experimental evidence. The simulations were able to replicate the effect of the thickness on the damage severity, clearly showing that it increases with decreasing thickness.

The validation of these parameters allowed the numerical predictions of the energy history, and the identification of the amount of dissipated energy through intralaminar damage, delamination and friction, for the 6-, 9-and 12-layers laminates. It was found that energy dissipation due to intralaminar damage outweighs the energy dissipated by delamination and friction, which can be caused by the high interlaminar fracture toughness along with the reduced in-plane strength of the tested laminates.

The findings of this study give the researchers the prospect of applying the same methodology to alternative lay-up configurations, materials, geometries, and/or boundary conditions in order to numerically analyze the impact response and identify the various damage mechanisms without recurring to experimental characterization.

References

[1] L. Ferreira, C. Coelho, P. Reis, Impact response of semi-cylindrical composite laminate shells under repeated low-velocity impacts, in: 2022 Advances in Science and Engineering Technology International Conferences (ASET), 2022, pp. 1–5. doi:10.1109/ASET53988.2022.9735043.

[2] M. De Moura, A. Marques, Prediction of low velocity impact damage in carbon–epoxy laminates, Composites Part A: Applied Science and Manufacturing 33 (3) (2002) 361–368. doi:10.1016/S1359-835X(01)00119-1.

[3] P. Reis, J. Ferreira, F. Antunes, M. Richardson, Effect of interlayer delamination on mechanical behavior of carbon/epoxy laminates, Journal of Composite Materials 43 (22) (2009) 2609–2621. doi:10.1177/0021998309344649.

[4] A. M. Amaro, P. N. Reis, M. F. de Moura, Residual strength after low velocity impact in carbon-epoxy laminates, in: Advanced Materials Forum III, Vol. 514 of Materials Science Forum, Trans Tech Publications Ltd, 2006, pp. 624–628. doi:10.4028/www.scientific.net/MSF.514-516.624.

[5] A. M. Amaro, P. N. B. Reis, M. F. S. F. de Moura, Delamination effect on bending behaviour in carbon–epoxy composites, Strain 47 (2) (2011) 203–208. doi:https://doi.org/10.1111/j.1475-1305.2008.00520.x.

[6] Impact response of kevlar composites with filled epoxy matrix, Composite Structures 94 (12) (2012) 3520–3528. doi:https://doi.org/10.1016/j.compstruct.2012.05.025.

[7] T. J. Kang, C. Kim, Energy-absorption mechanisms in kevlar multiaxial warp-knit fabric composites under impact loading, Composites Science and Technology 60 (5) (2000) 773–784. doi:https://doi.org/10.1016/S0266-3538(99)00185-2.

[8] G. Marom, E. Drukker, A. Weinberg, J. Banbaji, Impact behaviour of carbon/kevlar hybrid composites, Composites 17 (2) (1986) 150–153. doi:https://doi.org/10.1016/0010-4361(86)90253-3.

[9] J. Gustin, A. Joneson, M. Mahinfalah, J. Stone, Low velocity impact of combination kevlar/carbon fiber sandwich composites, Composite Structures 69 (4) (2005) 396–406. doi:https://doi.org/10.1016/j.compstruct.2004.07.020.

[10] F. Xia, X. Wu, Work on low-velocity impact properties of foam sandwich composites with various face sheets, Journal of Reinforced Plastics and Composites 29 (7) (2010) 1045–1054. doi:10.1177/0731684409102749.

[11] A. P. Sharma, S. H. Khan, R. Velmurugan, Effect of through thickness separation of fiber orientation on low velocity impact response of thin composite laminates, Heliyon 5 (10) (2019) e02706. doi:https://doi.org/10.1016/j.heliyon.2019.e02706.

[12] S. J. Kim, N. S. Goo, T. W. Kim, The effect of curvature on the dynamic response and impact-induced damage in composite laminates, Composites Science and Technology 57 (7) (1997) 763–773. doi:10.1016/S0266-3538(97)80015-2.

[13] S.-C. Her, Y.-C. Liang, The finite element analysis of composite laminates and shell structures subjected to low velocity impact, Composite Structures 66 (1-4) (2004) 277–285.

[14] K. Krishnamurthy, P. Mahajan, R. Mittal, Impact response and damage in laminated composite cylindrical shells, Composite structures 59 (1) (2003) 15–36.

[15] I. H. Choi, Finite element analysis of low-velocity impact response of convex and concave composite laminated shells, Composite Structures 186 (2018) 210–220. doi:10.1016/j.compstruct.2017.11.090.

[16] K. Krishnamurthy, P. Mahajan, R. Mittal, A parametric study of the impact response and damage of laminated cylindrical composite shells, Composites Science and Technology 61 (12) (2001) 1655–1669, publisher: Elsevier.

[17] G. Zhao, C. Cho, Damage initiation and propagation in composite shells subjected to impact, Composite Structures 78 (1) (2007) 91–100, publisher: Elsevier.

[18] B. Arachchige, H. Ghasemnejad, A. T. Augousti, Theoretical approach to predict transverse impact response of variable-stiffness curved composite plates, Composites Part B: Engineering 89 (2016) 34–43, publisher: Elsevier.

[19] L. S. Kistler, A. M. Waas, Experiment and Analysison the Response of Curved Laminated Composite Panels Subjected to Low Velocity Impact, International journal of impact engineering 21 (9) (1998) 711–736, publisher: Elsevier.

[20] S. Kumar, Analysis of impact response and damage in laminated composite shell involving large deformation and material degradation, Journal of Mechanics of Materials and Structures 3 (9) (2008) 1741–1756, publisher: Mathematical Sciences Publishers.

[21] Y. Zhou, Y. Sun, T. Huang, W. Cai, Sph-fem simulation of impacted composite laminates with different layups, Aerospace Science and Technology 95 (2019) 105469. doi:https://doi.org/10.1016/j.ast.2019.105469.

[22] G. Zhao, C. Cho, On Impact Damage of Composite Shells by a Low-Velocity Projectile, Journal of Composite Materials 38 (14) (2004) 1231–1254. doi:10.1177/0021998304042084.

[23] L. M. Ferreira, E. Graciani, F. París, Predicting failure load of a non-crimp fabric composite by means of a 3D finite element model including progressive damage, Composite Structures 225 (2019) 111115. doi:10.1016/j.compstruct.2019.111115.

[24] L. Ferreira, C. Coelho, Modelling progressive damage in ncf composites using the continuum damage mechanics method, in: 2022 Advances in Science and Engineering Technology International Conferences (ASET), 2022, pp. 1–4. doi:10.1109/ASET53988.2022.9734944.

[25] M. Richardson, M. Wisheart, Review of low-velocity impact properties of composite materials, Composites Part A: Applied Science and Manufacturing 27 (12) (1996) 1123–1131. doi:10.1016/1359-835X(96)00074-7.

[26] A. User, VUMAT for fabric reinforced composites, Dassault Systèmes (2008).

[27] A. Johnson, A. Pickett, P. Rozycki, Computational methods for predicting impact damage in composite structures, Composites Science and Technology 61 (15) (2001) 2183–2192. doi:10.1016/S0266-3538(01)00111-7.

[28] X. Liu, K. Rouf, B. Peng, W. Yu, Two-step homogenization of textile composites using mechanics of structure genome, Composite Structures 171 (2017) 252–262. doi:https://doi.org/10.1016/j.compstruct.2017.03.029.

[29] P. Reis, P. Sousa, L. Ferreira, C. Coelho, Multi-impact response of semi-cylindrical composite laminated shells with different thicknesses, Composite Structures 310 (2023) 116771. doi:10.1016/j.compstruct.2023.116771.

[30] L. M. Ferreira, C. A. C. P. Coelho, P. N. B. Reis, Numerical simulations of the low-velocity impact response of semicylindrical woven composite shells, Materials 16 (9) (2023). doi:10.3390/ma16093442.

[31] L. M. Ferreira, C. A. C. P. Coelho, P. N. B. Reis, Effect of cohesive properties on low-velocity impact simulations of woven composite shells, Applied Sciences 13 (12) (2023) 6948. doi:10.3390/app13126948.

[32] T. Tay, G. Liu, V. Tan, X. Sun, D. Pham, Progressive Failure Analysis of Composites, Journal of Composite Materials 42 (18) (2008) 1921–1966. doi:10.1177/0021998308093912.

[33] R. Bogenfeld, J. Kreikemeier, T. Wille, Review and benchmark study on the analysis of low-velocity impact on composite laminates, Engineering Failure Analysis 86 (2018) 72–99. doi:10.1016/j.engfailanal.2017.12.019.

[34] P. P. Camanho, C. G. Dávila, Mixed-mode decohesion finite elements for the simulation of delamination in composite materials, NASA/TM-202-211737 (2002).

[35] M. Benzeggagh, M. Kenane, Measurement of mixed-mode delamination fracture toughness of unidirectional glass/epoxy composites with mixed-mode bending apparatus, Composites Science and Technology 56 (4) (1996) 439–449. doi:10.1016/0266-3538(96)00005-X.

[36] D. Systemes, ABAQUS.
URL https://www.3ds.com/products-services/simulia/products/abaqus/

[37] P. Ladeveze, E. LeDantec, Damage modelling of the elementary ply for laminated composites, Composites Science and Technology 43 (3) (1992) 257–267. doi:10.1016/0266-3538(92)90097-M.

[38] V. Kostopoulos, Y. Markopoulos, G. Giannopoulos, D. Vlachos, Finite element analysis of impact damage response of composite motorcycle safety helmets, Composites Part B: Engineering 33 (2) (2002) 99–107. doi:10.1016/S1359-8368(01)00066-X.

[39] Utilization of composite's tensile properties for energy absorbing systems, Composite Structures 75 (1) (2006) 29–38, thirteenth International Conference on Composite Structures. doi:https://doi.org/10.1016/j.compstruct.2006.04.081.

[40] Experimental investigation of the hydrostatic performance of fibre reinforced tubes, Appl Compos Mater 24 (2017) 417–448. doi:https://doi.org/10.1007/s10443-016-9563-7.

[41] X. Liu, W. Yu, TexGen4SC (Sep. 2016).
URL https://cdmhub.org/resources/texgen4sc

[42] H. Lin, L. P. Brown, A. C. Long, Modelling and Simulating Textile Structures Using TexGen, Advanced Materials Research 331 (2011) 44–47. doi:10.4028/www.scientific.net/AMR.331.44.

[43] C. A. Campos Pais Coelho, F. V. Navalho, P. Reis, Impact response of laminated cylindrical shells, Frattura ed Integrità Strutturale 13 (48) (2019) 411–418. doi:10.3221/IGF-ESIS.48.39.

[44] S. E. Systems, Sicomin Technical Datasheet., Tech. rep. (2014).
URL http://www.sicomin.com/datasheets/product-pdf39.pdf.

[45] M. P. Silva, P. Santos, J. M. Parente, S. Valvez, P. N. B. Reis, A. P. Piedade, Effect of Post-Cure on the Static and Viscoelastic Properties of a Polyester Resin, Polymers 12 (9) (2020). doi:10.3390/polym12091927.

[46] C. T. Technologie, Yarn Processing - Facts plied and texturized glass yarns.
URL https://textilglas.culimeta.de/fileadmin/user_upload/FACTS_Yarn_Processing_2019.pdf

[47] M. S. Hoo Fatt, C. Lin, Perforation of clamped, woven E-glass/polyester panels, Composites Part B: Engineering 35 (5) (2004) 359–378. doi:10.1016/j.compositesb.2003.04.001.

[48] L. Alonso, F. Martínez-Hergueta, D. Garcia-Gonzalez, C. Navarro, S. García-Castillo, F. Teixeira-Dias, A finite element approach to model high-velocity impact on thin woven GFRP plates, International Journal of Impact Engineering 142 (2020) 103593. doi:10.1016/j.ijimpeng.2020.103593.

[49] S. Sridharan, M. Pankow, Performance evaluation of two progressive damage models for composite laminates under various speed impact loading, International Journal of Impact Engineering 143 (2020) 103615. doi:10.1016/j.ijimpeng.2020.103615.

[50] V. Bodepati, K. Mogulanna, G. S. Rao, M. Vemuri, Numerical Simulation and Experimental Validation of E-Glass/epoxy Composite Material under Ballistic Impact of 9 mm Soft Projectile, Plasticity and Impact Mechanics 173 (2017) 740–746. doi:10.1016/j.proeng.2016.12.068.

[51] A. Esnaola, B. Elguezabal, J. Aurrekoetxea, I. Gallego, I. Ulacia, Optimization of the semi-hexagonal geometry of a composite crush structure by finite element analysis, Composites Part B: Engineering 93 (2016) 56–66. doi:10.1016/j.compositesb.2016.03.002.

[52] L. Daudeville, O. Allix, P. Ladevèze, Delamination analysis by damage mechanics: Some applications, Composites Engineering 5 (1) (1995) 17–24. doi:10.1016/0961-9526(95)93976-3.

[53] Z. Zou, S. Reid, S. Li, A continuum damage model for delaminations in laminated composites, Journal of the Mechanics and Physics of Solids 51 (2) (2003) 333–356. doi:10.1016/S0022-5096(02)00075-3.

[54] P. P. Camanho, C. G. Davila, M. F. de Moura, Numerical Simulation of Mixed-Mode Progressive Delamination in Composite Materials, Journal of Composite Materials 37 (16) (2003) 1415–1438. doi:10.1177/0021998303034505.

[55] A. Turon, C. Dávila, P. Camanho, J. Costa, An engineering solution for mesh size effects in the simulation of delamination using cohesive zone models, Engineering Fracture Mechanics 74 (10) (2007) 1665–1682. doi:10.1016/j.engfracmech.2006.08.025.

[56] K. Song, C. G. Dávila, C. A. Rose, Guidelines and parameter selection for the simulation of progressive delamination, Vol. 41, 2008, pp. 43–44.

[57] K.-H. Nguyen, H.-W. Ju, V.-H. Truong, J.-H. Kweon, Delamination analysis of multi-angle composite curved beams using an out-of-autoclave material, Composite Structures 183 (2018) 320–330. doi:10.1016/j.compstruct.2017.03.078.

[58] A. M. Amaro, P. N. B. Reis, A. G. Magalhães, M. F. S. F. de Moura, The Influence of the Boundary Conditions on Low-Velocity Impact Composite Damage, Strain 47 (s1) (2011) e220–e226. doi:10.1111/j.1475-1305.2008.00534.x.

[59] S. Heimbs, T. Bergmann, D. Schueler, N. Toso-Pentecôte, High velocity impact on preloaded composite plates, Composite Structures 111 (2014) 158–168. doi:10.1016/j.compstruct.2013.12.031.

[60] G. Kinvi-Dossou, R. Matadi Boumbimba, N. Bonfoh, Y. Koutsawa, D. Eccli, P. Gerard, A numerical homogenization of E-glass/acrylic woven composite laminates: Application to low velocity impact, Composite Structures 200 (2018) 540–554. doi:10.1016/j.compstruct.2018.05.137.

[61] R. Batra, G. Gopinath, J. Zheng, Damage and failure in low energy impact of fiber-reinforced polymeric composite laminates, Composite Structures 94 (2) (2012) 540–547. doi:10.1016/j.compstruct.2011.08.015.

[62] J. Schön, Coefficient of friction of composite delamination surfaces, Wear 237 (1) (2000) 77–89. doi:10.1016/S0043-1648(99)00315-4.

[63] L. Bresciani, A. Manes, A. Ruggiero, G. Iannitti, M. Giglio, Experimental tests and numerical modelling of ballistic impacts against Kevlar 29

plain-woven fabrics with an epoxy matrix: Macro-homogeneous and Meso-heterogeneous approaches, Composites Part B: Engineering 88 (2016) 114–130. doi:10.1016/j.compositesb.2015.10.039.

[64] D. Liu, Impact-Induced Delamination—A View of Bending Stiffness Mismatching, Journal of Composite Materials 22 (7) (1988) 674–692. doi:10.1177/002199838802200706.

[65] O. David-West, D. Nash, W. Banks, An experimental study of damage accumulation in balanced CFRP laminates due to repeated impact, Composite structures 83 (3) (2008) 247–258.

[66] T. Gómez-del Rıo, R. Zaera, E. Barbero, C. Navarro, Damage in CFRPs due to low velocity impact at low temperature, Composites Part B: Engineering 36 (1). doi:10.1016/j.compositesb.2004.04.003.

[67] A. Amaro, P. Reis, M. de Moura, M. Neto, Influence of open holes on composites delamination induced by low velocity impact loads, Composite Structures 97 (2013) 239–244. doi:10.1016/j.compstruct.2012.09.041.